



Optics Letters

Focused anti-scatter grid for background reduction in x-ray fluorescence tomography

JAKOB C. LARSSON,*  KIAN SHAKER,  AND HANS M. HERTZ 

Biomedical and X-Ray Physics, Department of Applied Physics, KTH Royal Institute of Technology/Albanova, 10691 Stockholm, Sweden

*Corresponding author: jakob.larsson@biox.kth.se

Received 13 March 2018; revised 18 April 2018; accepted 30 April 2018; posted 1 May 2018 (Doc. ID 325960); published 24 May 2018

X-ray fluorescence (XRF) tomography is an emerging imaging technology with the potential for high spatial resolution molecular imaging. One of the key limitations is the background noise due to Compton scattering since it degrades the signal and limits the sensitivity. In this Letter, we present a linear focused anti-scatter grid that reduces the Compton scattering background. An anti-scatter grid was manufactured and evaluated both experimentally and theoretically with Monte Carlo simulations. The measurements showed a 31% increase in signal-to-background ratio, and simulations of an improved grid showed that this can easily be extended up to >75%. Simulated tomographies using the improved grid show a large improvement in reconstruction quality. The anti-scatter grid will be important for *in vivo* XRF tomography since the background reduction allows for faster scan times, lower doses, and lower nanoparticle concentrations. © 2018 Optical Society of America

OCIS codes: (110.7440) X-ray imaging; (170.7440) X-ray imaging; (110.6960) Tomography; (290.4210) Multiple scattering.

<https://doi.org/10.1364/OL.43.002591>

X-ray fluorescence (XRF) nanoparticle (NP) tomography is an emerging imaging technology with the potential for high-resolution molecular imaging [1–5]. One of the key limitations is background noise due to Compton scattering [2] since it degrades the signal and limits the sensitivity. In this Letter, we present a linear focused anti-scatter grid that effectively reduces the multiple Compton scattering background. A prototype was manufactured and evaluated both experimentally and with Monte Carlo simulations.

XRF NP tomography is a scanning x-ray imaging technique that uses targeted NPs as bio-markers for early tumor detection [2]. By measuring the XRF signal from the NPs, it is possible to reconstruct both the spatial distribution and the concentration of the NPs. Our imaging system combines a high-brightness liquid-metal-jet x-ray source, multilayer optics, photon-counting detectors, and spectrally matched molybdenum (Mo) NPs in order to minimize the background, reducing scan times and increasing sensitivity.

However, the background noise is still one of the major issues in XRF tomography since statistical variations in the background set an upper limit to the maximum sensitivity of the system. In addition, at very short exposure times and low concentrations, e.g., in tomography of tumors in mice [5], it is not possible to directly measure the background due to poor statistics and high photon noise. Therefore, the background has to be estimated which often results in either a loss of signal (too high estimate) or reconstruction artifacts (too low estimate). A large part of the background is caused by multiple Compton scattering from the main excitation beam. The scattered photons overlap spectrally with the fluorescence from the NPs, making them indistinguishable from the signal and, thus, reducing the signal-to-background ratio (SBR).

Anti-scatter grids are often used to reduce scattering in many imaging techniques, e.g., radiology and mammography [6,7], and computed tomography (CT) [8], but have not previously been used in XRF tomography. The grid can be designed in a number of ways, either linear or crossed, or planar or focused, and with different interspace and septa (grid bars) materials. Although one design using Bragg crystals has been proposed for XRF tomography [9], the setup is complex and results in a large loss of signal.

In this Letter, we manufactured and evaluated a linear focused anti-scatter grid for XRF tomography that effectively reduces the Compton background and improves the SBR. The grid was evaluated by measuring and comparing the SBR with and without the grid, both experimentally and theoretically using Monte Carlo simulations. Additional simulations of a full tomography were also performed using an improved grid, showing a large improvement in reconstruction quality.

Figure 1(a) depicts the experimental arrangement. It consists of a liquid-metal-jet microfocus x-ray source, focusing optics, the object, two photon-counting detectors, and the anti-scatter grid. The source (D2, Excillum AB, Sweden) uses a jet of galinstan (an alloy of Ga/In/Sn) as a target, producing characteristic line emission at the In K_{α} line at 24.1 keV. It operates at 120 kVp/170 W giving a flux of 6×10^{11} ph/(s × sr) in the In K_{α} line.

The focusing optics is a double-bounce grazing-incidence multilayer Montel mirror (ELM61, Incoatec GmbH, Germany), optimized for the In K_{α} line at 24.1 keV. It

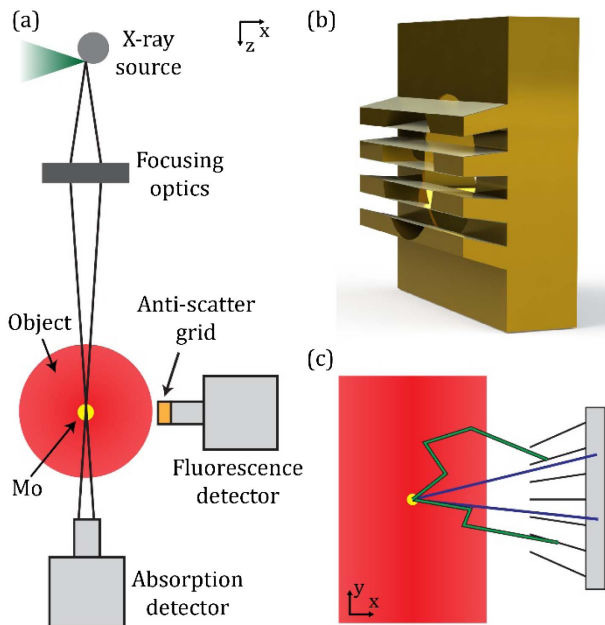


Fig. 1. (a) Overview of the imaging system. (b) 3D rendering of the anti-scatter grid. The grid consists of seven tungsten grid bars supported by a copper baseplate. (c) Side view of the object and anti-scatter grids. Multiple scattered photons (green) are blocked by the grid, while the primary photons (blue) enter the detector.

produces a semi-monochromatic pencil beam with a $\sim 100 \times 100 \mu\text{m}^2$ full width at half-maximum (FWHM) focus located 56 cm from the source. The brilliance in the focus was measured to $8 \times 10^8 \text{ ph}/(\text{s} \times \text{mrad}^2 \times \text{mm}^2 \times \text{line})$.

The object used to evaluate the grid is a 20 mm diameter mouse-equivalent phantom made of polyethylene terephthalate (PET/Mylar). It has a 2 mm diameter hole that can be filled with a Mo solution. Mo has its K absorption edge at 20.0 keV and produces K_{α} XRF at 17.4 keV.

The two detectors measure the attenuation of the direct beam (absorption CT) and the fluorescence signal. The absorption detector is a 25 mm^2 CdTe spectrometer (X123-CdTe, Amptek Inc., MA), and the fluorescence detector is a 17 mm^2 silicon-drift detector (X123-SDD, Amptek Inc., MA) with 260 eV energy resolution at 17.4 keV. The anti-scatter grid is placed directly in front of the fluorescence detector, 18.5 mm from the pencil beam.

Figure 1(b) shows a 3D rendering of the anti-scatter grid. It is a linear focused grid consisting of seven horizontal tungsten septa (grid bars) angled to focus on line 18.5 mm in front of the detector. Each septum is $35 \mu\text{m}$ thick and 3 mm long with a spacing of 1.5 mm, giving a grid ratio of 2:1. The latter is defined as the ratio between the height and interspace of the septa. No filler material is used, but the septa are supported by a copper baseplate. The anti-scatter grid was manufactured in two steps. First, the supporting copper baseplate was created using a wire-cut electrical discharge machine. Secondly, the tungsten septa were taped directly on top of the support structures.

Figure 1(c) illustrates the main principle of the anti-scatter grid. Primary photons (both fluorescence and direct scattering) pass through the grid to the fluorescence detector, while multiple scattered photons are absorbed.

Simulations of the imaging system and anti-scatter grid were performed using an in-house Monte Carlo simulation software, XRF-GPU [10]. The software is based on the open-source MC-GPU [11], a Monte Carlo simulation tool for x-ray transport parallelized on the GPU for fast computations. To the best of our knowledge, XRF-GPU is the only Monte Carlo tool specifically developed for providing fast XRF tomography simulations with high accuracy. In addition to modifying the original code to accommodate for the acquisition geometry used in our experimental arrangement, the simulation of fluorescence has been implemented, as well as an anti-scatter grid with flexible parameters. For each step in a tomography, an artificial grid is simulated by calculating the position and tilt of the grid elements relative to the detector. These are then used to determine, given the position and direction of a photon exiting the phantom, how much grid material it has to pass before it reaches the detector. This is used, together with the specified grid material and density, to calculate the probability of grid-absorption. In the case of the latter, the photon is stored separately from those absorbed in the detector. This allows simulating both scenarios (with and without grid) simultaneously.

The prototype grid was evaluated experimentally and by simulations by measuring the difference in SBR with and without the grid in a single spectrum. For the measured spectra, the grid was first aligned with the pencil beam by placing the fluorescence detector on a $y-z$ stage and optimizing for maximum signal intensity. Two spectra, with ($\bar{I}_w(E)$) and without ($\bar{I}_{w/o}(E)$) grid, were then acquired by letting the x-ray pencil beam traverse through the center of the PET phantom and the 2 mm diameter hole filled with 0.005 wt. % (0.05 mg/g) Mo ICP standard. In order to accurately separate the XRF signal, S , and scattering background, B , two spectra of the background (2 mm hole filled with water) were also acquired ($\bar{B}_w(E)$ and $\bar{B}_{w/o}(E)$). The exposure time was set to 3600 s in order to minimize the photon noise. The measured intensity, $I = S + B$, and background, B , was extracted by integrating the respective spectra within the FWHM of the fluorescence peak at 17.4 keV and the SBR calculated as

$$\text{SBR}_i = (I_i - B_i)/B_i, i = \{w, w/o\}. \quad (1)$$

The simulations were performed using the same experimental arrangement and acquisition parameters. Only one exposure had to be simulated since the software simulates both cases (with and without grid) simultaneously and stores the signal and background separately. In this case, the SBR was calculated as

$$\text{SBR}_{\text{sim},i} = S_i/B_i, i = \{w, w/o\}. \quad (2)$$

Figure 2(a) displays the measured and simulated spectra. The inset shows an enhanced view over the fluorescence signal between 17 and 18 keV. As can be seen, the simulations show excellent agreement with the measurements over the whole spectrum. The $\text{SBR}_{w/o}$ was measured to 1.23 ± 0.02 and SBR_w to 1.62 ± 0.03 , giving an increase in SBR by $31\% \pm 3\%$ when using the grid. The simulations gave slightly lower values for the grid ($\text{SBR}_{\text{sim},w} = 1.22 \pm 0.02$, $\text{SBR}_{\text{sim},w/o} = 1.54 \pm 0.03$, $\Delta\text{SBR} = 27\% \pm 3\%$) which is most likely due to non-perfect agreement in the simulated pencil beam spectrum. Furthermore, the measurements showed that 10% of the primary signal was absorbed by the grid, compared to 7% in the simulations. This is likely caused by

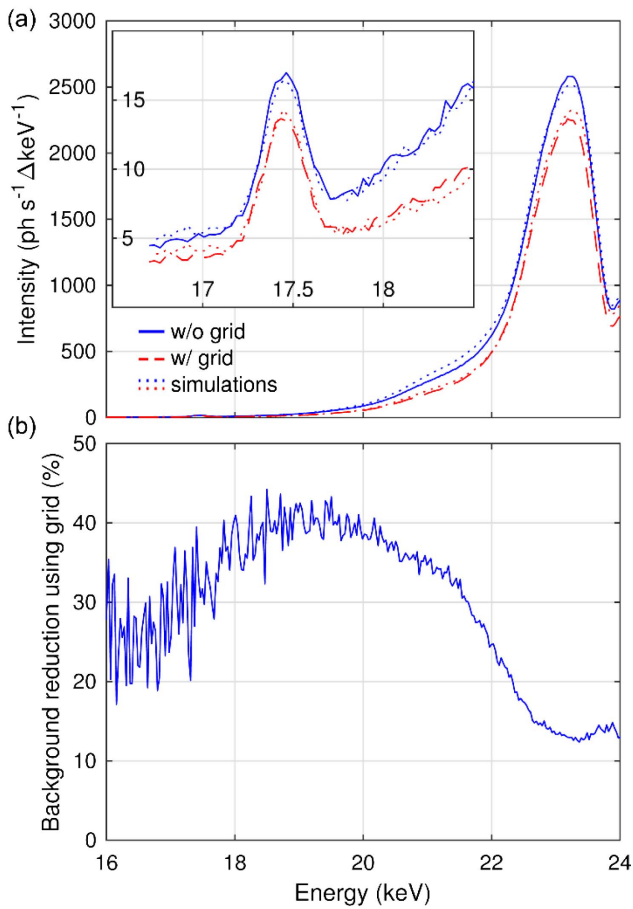


Fig. 2. (a) Measured and simulated spectra with and without the anti-scatter grid. The inset shows an enhanced view over the XRF signal. (b) Background reduction using the anti-scatter grid as a function of energy.

alignment errors in the positioning of the grid. Figure 2(b) shows the background reduction using the anti-scatter grid as a function of energy. The grid does not block primary scattered photons so the primary Compton scattering peak at 23 keV is reduced by a similar amount as the Mo fluorescence signal. Going downwards in energy, the background reduction increases due to absorption of multiple scattering. However, at 18 keV, the trend is reversed. The reason for this is that the amplitude of the multiple Compton scattering reduces to such a degree that other sources of noise, e.g., detector noise, start playing a role. This indicates that the anti-scatter grid might be more effective for other bio-markers than Mo such as Ru or Rh which have their K_{α} emission lines at 19.3 and 20.2 keV, respectively.

To further illustrate the potential of the anti-scatter grid, a full XRF tomography was simulated with and without an improved grid. The improved grid consists of 15 tungsten septa, each 20 μm thick and 7 mm long with a spacing of 0.75 mm, giving a grid ratio of 9:1 (see 2:1 for the prototype). All parameters were chosen to be realizable with the current grid design. The SBR analysis was performed again, showing an increase in SBR by $77\% \pm 5\%$.

The design of the improved grid is based on a preliminary simulation study which investigated the effects of each

parameter. In general, the septa should be thin to prevent absorption of the primary photons, but thick enough to absorb the scattered photons. To minimize this trade-off, a high- Z material (W in this case) should be used for the septa. A smaller interspace distance (i.e., higher grid ratio) significantly reduced the scattering, but also increased the absorption of the primary photons. This Letter suggests that the optimal septa height is highly dependent on the object and its position relative to the detector. Finding the optimal parameters is a complex task which we leave as a future study, and we expect even better performance to be reported following that.

Figure 3(a) shows the simulated object used for the tomography. It is a 20 mm diameter PET phantom with six holes of different diameters (350–550 μm) filled with a 0.01 wt. % (0.1 mg/g) Mo solution. This concentration is 10 \times lower compared to what has previously been observed in tumors with passive NP targeting [4,12]. The combination of sizes and concentrations was chosen in order to be close to the detection limit of our system.

The tomography was simulated by scanning the object in 200 μm steps at multiple angles, giving 180 projections over 180°. In each step, both the attenuation of the pencil beam

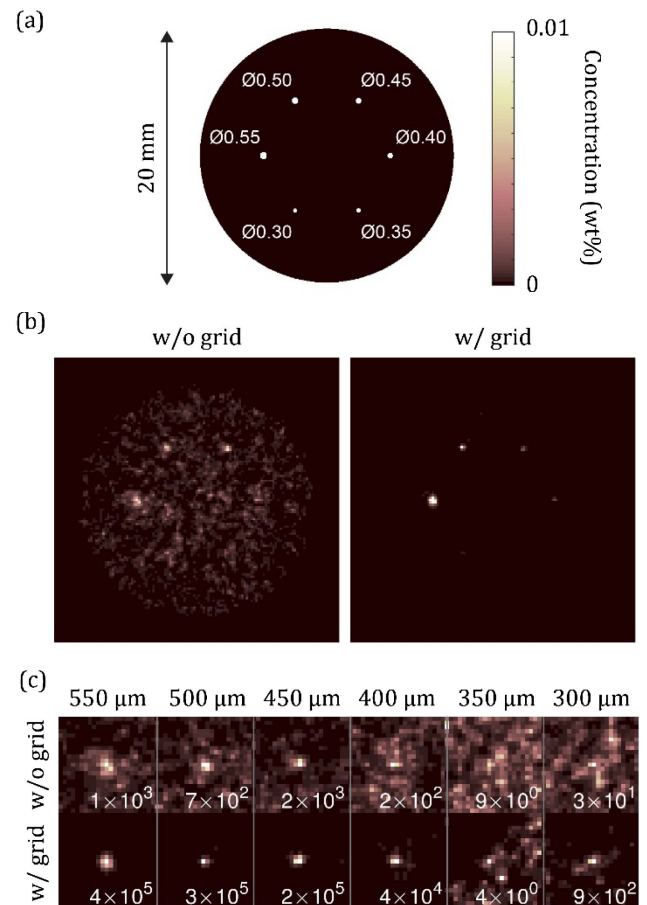


Fig. 3. (a) Phantom used for tomography simulations. It is a 20 mm diameter PET cylinder with six holes, 300–550 μm , filled with a 0.01 wt. % Mo solution. (b) Reconstructed images of a tomography without and with an optimized anti-scatter grid. (c) Comparison of the reconstructed signal. The numbers are the SNR^2 calculated according to the Rose criterion.

(regular CT) and the fluorescence signal were measured. The number of simulated photons was set to correspond to an acquisition time of 200 ms per step. The simulated data were then reconstructed using an in-house iterative reconstruction algorithm that accounts for both self-absorption of the pencil beam and self-absorption of the fluorescence signal to the detector [5]. Since both datasets (with and without grid) are extracted from the same Monte Carlo simulation, they both have the same statistical variations. The only difference is that some photons are blocked by the anti-scatter grid before entering the detector. This makes it easier to compare the two reconstructions since any differences due to photon noise can be neglected.

Figure 3(b) shows the reconstructed images with and without anti-scatter grid. The contrast is set between 0 and 0.01 wt. % according to the color bar in Fig. 3(a). As can be seen, the background is greatly reduced when using the anti-scatter grid. Although the four larger holes are visible in both images, the anti-scatter grid greatly reduces the risk of false-positives. Figure 3(c) shows a quantitative analysis of the observability [13] for each hole, where the numbers indicate the signal-to-noise ratio (SNR²). An SNR² of ~25 is required for a feature to be distinguishable by the human eye [14]. In general, the SNR² is several orders of magnitude larger for the reconstruction with the anti-scatter grid, mainly due to the reduced background. The 350 μm hole is not visible in any of the reconstructions due to a low signal and large photon noise. The smallest hole is barely above the detection limit without the grid (SNR² = 30), but is clearly visible with the grid (SNR² = 900).

It should be noted that the anti-scatter grid has the largest impact at low signal levels. When the signal is much larger than the background, the background noise and background subtraction have negligible effect on the reconstruction.

In conclusion, we have manufactured an anti-scatter grid for XRF tomography that gives a 31% increase in SBR. Monte Carlo simulations show that tuning the grid parameters can easily push this up to >75%. Furthermore, simulated tomographies using the improved grid illustrate the benefits of using

the anti-scatter grid at low signal levels. The anti-scatter grid will be important for *in vivo* XRF tomography since the background reduction allows for faster scan times, lower doses, and lower NP concentrations.

Funding. The Wallenberg Foundation.

Acknowledgment. The authors would like to thank Carmen Vogt for preparing the Mo solutions and Bosse Barksäter in the mechanical workshop for manufacturing the anti-scatter grid.

REFERENCES

1. M. Bazalova, Y. Kuang, G. Pratz, and L. Xing, *IEEE Trans. Med. Imaging* **31**, 1620 (2012).
2. H. M. Hertz, J. C. Larsson, U. Lundström, D. H. Larsson, and C. Vogt, *Opt. Lett.* **39**, 2790 (2014).
3. M. Ahmad, G. Pratz, M. Bazalova, and L. Xing, *IEEE Access* **2**, 1051 (2014).
4. N. Manohar, F. J. Reynoso, P. Diagaradjane, S. Krishnan, and S. H. Cho, *Sci. Rep.* **6**, 22079 (2016).
5. J. C. Larsson, C. Vogt, W. Vågberg, M. S. Toprak, J. Dzieran, M. Arsenian-Henriksson, and H. M. Hertz, Submitted.
6. J. T. Bushberg, J. A. Siebert, E. M. Leidholdt, Jr., and J. M. Boone, in *The Essential Physics of Medical Imaging*, 2nd ed. (Lippincott Williams & Wilkins, 2002), p. 168.
7. J. T. Dobbins III, in *Handbook of Medical Imaging, Volume 1. Physics and Psychophysics* (SPIE, 2000), p. 176.
8. P. Suetens, in *Fundamentals of Medical Imaging*, 2nd ed. (Cambridge University, 2009), p. 54.
9. B. H. Müller, C. Hoeschen, F. Grüner, V. A. Arkadiev, and T. R. C. Johnson, *Phys. Med. Biol.* **58**, 8063 (2013).
10. K. Shaker, "GPU Monte-Carlo simulation of x-ray fluorescence tomography," Master's thesis (KTH, 2017).
11. A. Badal and A. Badano, *Med. Phys.* **36**, 4878 (2009).
12. J. F. Hainfeld, D. N. Slatkin, T. M. Focella, and H. M. Smitowitz, *Br. J. Radiol.* **79**, 248 (2006).
13. U. Lundström, D. H. Larsson, A. Burvall, P. A. C. Takman, L. Scott, H. Brismar, and H. M. Hertz, *Phys. Med. Biol.* **57**, 2603 (2012).
14. A. Rose, *J. Opt. Soc. Am.* **38**, 196 (1948).